Dalton Transactions

Accepted Manuscript

ROYAL SOCIETY OF CHEMISTRY

www.rsc.org/dalton

Graphical Abstract

A prominent enhanced photocatalytic ability of the MoS_2@CuO heterojunction and a better response/recover times were obtained. The first-principles calculation showed that water molecule can bind stronger to CuO surface in comparison with MoS_2, in line with the experimental observations.

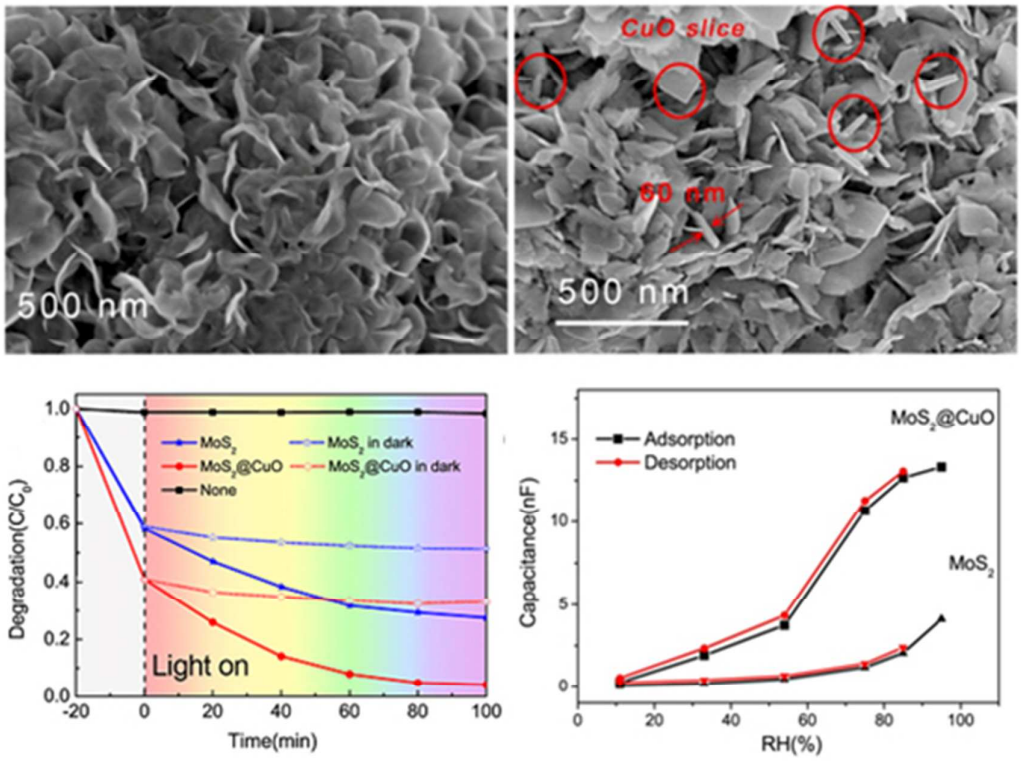

Journal Name

ARTICLE

Synthesis of MoS_2@CuO Heterogeneous Structure with Improved Photocatalysis Performance and H_2O Adsorption Analysis

Received 00th January 20xx,
Accepted 00th January 20xx

DOI: 10.1039/x0xx00000x

www.rsc.org/

Honglin Li, Ke Yu*, Xiang Lei, Bangjun Guo, Chao Li, Hao Fu and Ziqiang Zhu

MoS_2@CuO heterogeneous structure nanoflowers were synthesized through two-step hydrothermal method for the first time. The valence band offset (VBO) and conduction band offset (CBO) of MoS_2@CuO heterojunction, the bases for the design of heterogeneous structure, were determined by X-ray photoemission spectroscopy (XPS). For the increased specific surface area and the formation of staggered type-II band alignment of the composite structure, a significant enhanced photocatalytic ability of the MoS_2@CuO heterojunction was obtained by studying the photodegradation of methylene blue (MB). After irradiation for 100 min, the residual MB in solution was about 27.5 % for pristine MoS_2 nanoflowers while 4.3 % for MoS_2@CuO hetero-nanoflowers, respectively. The humidity sensing properties of the two nanostructures were also studied as a comparison. The results showed that better response/recover times were obtained. In order to give a theoretical explanation for this phenomenon, we performed the first-principles calculation to analyse the corresponding humidity sensing mechanisms of MoS_2 and MoS_2@CuO in detail. The calculated results showed that water molecule could bind stronger to CuO surface compared to MoS_2, which in line with the experimental observations.

1 Introduction

Over the past few years, the discovery of 2-dimensional graphene has triggered extensive studies on the 2-dimensional materials due to their potential applications in electrical, mechanical and optical devices.[1] Recently, an increasing number of researchers are paying close attention to MoS_2 for it layered nanostructure.[2] Experimentally and theoretically, MoS_2 based materials have been extensively studied, showing great promise for use in many applications, such as lithium batteries, catalysts, and lubricants.[3] MoS_2 is built up by weak van-der-Waals force of adjacent atomic sandwiches units. Each stable unit is consisted by a hexagonal plane of Mo atoms and two S atoms hexagonal planes modulated by covalent interactions in the form of a trigonal prismatic form. Until now, photocatalytic property of MoS_2 has not been fully applied in industry for its rapid recombination rate of photogenerated electrons and holes.[4]

Cupric oxide (CuO) is a p-type semiconductor with an indirect band gap. It has received much attention because it has outstanding photoconductive and photochemical properties.[5] CuO is a good choice among the numerous catalysts, and it has utilized as a co-catalyst to extend the region of visible-light response.[6] When it is hybridized with n-type MoS_2, the staggered type-II band alignment should take shape and facilitate the utilization of optical energy. The previous studies proved that the heterogeneous structures were in favour of the improvement of many performances, including photoluminous, catalysis and sensing for the formation of new band alignment form, change of surface state, enlarged specific surface area and so on.[7, 8] Since the band offset of the interface can form potential barrier, it may hinder the flow of photo-generated electrons and cause energy loss, therefore, it is necessary to know the band alignment of the corresponding heterojunction systems. In this paper, we detailedly study the band offsets between MoS_2 and CuO synthesized by hydrothermal method through XPS. The obtained VBO and CBO are smaller than the other reported heterogeneous structures, which encourages us to applied this heterojunction structure to the photocatalysis application. Besides, humidity sensors also have many critical applications, such as in agriculture, meteorology and medical field.[9] CuO has been extensively investigated for its unique sensing characteristics.[10, 11] In spite of many semiconductor,[12] glass-ceramic[13] and polymer[14] have been extensively researched for humidity sensor utilizations, much more researches are demanded to optimize the sensor' performance parameters, such as response/recovery times. Many novel materials (for example, composite materials) remain to be explored. Based on these considerations, we are enlightened to study the corresponding humidity sensing properties of this composite structure and present a set of analytical methods. We believe this meaningful work would provide a certain theoretical guidance for the research of hybrid materials in the further.

In this paper, we synthesised MoS_2@CuO hetero-nanoflowers composite for the first time and proposed a facile route to fabricate the composite based on MoS_2 nanoflowers

Key Laboratory of Polar Materials and Devices (Ministry of Education of China), Department of Electronic Engineering, East China Normal University, Shanghai, 200241, P. R. China.
**Corresponding Author: yk5188@263.net*

through a two-step hydrothermal method. The experimental conditions were simple and controllable and the related reagents were simple and easy to get. The mechanism of the obtained heterogeneous structure in photocatalysis and humidity sensor were discussed in detail. We evaluated the photocatalytic and humidity sensing abilities of MoS_2@CuO hetero-nanoflowers and compared it with the pristine MoS_2 structure. Moreover, we also conducted a systematic study of the adsorption of water molecule on MoS_2/CuO surfaces based on first-principles calculation. The corresponding electronic structures and charge transfer characteristics revealed that there existed different charge transfer mechanisms, which inevitably had different influence on their humidity sensing behaviours.

2 Experimental section

2.1 Synthesis of MoS_2@CuO hetero-nanoflowers

The experimental procedures for the synthesis of MoS_2 nanoflowers through hydrothermal route were described as follows: 1.2 g sodium molybdate dihydrate and 1.6 g thioacetamide were used as Mo an S sources, respectively, and were dissolved in 80 ml deionized water. Then 0.6 g oxalic acid was added to the above mixed liquor to adjust the pH value to an acid environment. After magnetic stirring for 30 min, a transparent solution formed and transferred to a 100 ml stainless-steel autoclave with a Teflon liner. Finally, the autoclave was sealed and heated at drying oven in 200 ℃ for 24 h without shaking or stirring during this period of time. After autoclave naturally cooled down to room temperature, black products were attached to the inner wall. These black resultants were washed with distilled water several times to remove any impurities, then they were dried in a vacuum at 60 ℃ for 6 h to obtain black powders. All chemical reagents directly used here were analytical grade and without a further purification. For the synthesis of MoS_2@CuO hetero-nanoflowers, 0.1 g MoS_2 as-fabricated the above was dissolved in 80 ml deionized water and stirred well to ensure MoS_2 nanoflowers were completely dispersed in the deionized water. Then, 0.02 g copper nitrate trihydrate was added to the above solution. After magnetic stirring the mixed liquor for 30 min, the suspension was obtained and transferred into a stainless steel autoclave with Teflon-lined and heated at 120 ℃ for 2 h. Then the resultant was annealed at 350 °C for 2 h in flowing pure argon.

2.2 Characterization

The lattice structures of the different samples were characterized by X-ray diffraction (D8 Advance/ BRUKER AXS GMBH) with Cu-Kα radiation (λ=0.1541 nm). The diffraction data were collected in the 2θ scanning ranging from 10° to 70° with 0.02° per step. The morphologies of the samples were obtained by field emission scanning electron microscopy (FESEM, JEOL-JSM-6700F) at an accelerating voltage of 20 kV and transmission electron microscopy (TEM, JEOL-JEM-2100) at an accelerating voltage of 200 kV. The samples used for TEM characterization were prepared by dropping the colloidal solution to a holey carbon-coated copper grid, which then were dried in air. XPS was performed with an ESCALAB 250Xi instrument.

2.3 Photocatalytic measurements

MB was chosen to evaluate the photodegradation performance of the prepared nanostructures in this section for it has strong adsorption to catalyst surfaces, specific optical absorption and well resistance to light degradation. The monitor wavelength of the photodegradation was at 664 nm which is the highest optical absorption of MB. The photocatalysis capacities of pristine MoS_2 and MoS_2@CuO samples were evaluated by MB degradation under UV-vis light at room temperature. The photocatalysts were added to 100 mL MB aqueous solution. Then, the suspension was stirred for 20 min in dark environment before degradation to establish the adsorption/desorption equilibrium. To eliminate the possible thermal effect, the reactor was situated in a glass container that cooled by flowing water. Then, the mixed solution was irradiated for 100 min and the absorption was measured by a UV-vis spectrophotometer (UNICO 2802) every 20 minutes.

In this work, a single surface photovoltage (SPV) signal was measured after illumination to assess the photocatalytic performance of different structures. The same light source employed in all photocatalytic tests was used here in the corresponding measurements, which would suit for a reasonable study of the relation between SPV and photocatalysis. In order to obtain exact SPV values, three independent measurements were conducted and averaged. Total organic carbon (TOC) analyzer (AnalytikJena, Multi N/C 2100S) was employed to analyze the mineralization degree of the corresponding solutions.

2.4 Humidity sensing measurement

The humidity sensors were composed by the interdigital electrode with sensing materials film on the surfaces. The glass sheet substrates were cleaned in a sonication bath and the interdigital silver paste electrodes were deposited on the glass substrate. The MoS_2 and MoS_2@CuO suspension were dispersed by ultrasonic and coated on the glass substrate with the electrode to form a thin film as a humidity sensing layer. Then the sensors were dried at 50 ℃ for 6 h. The specific humidity environments were provided by saturated aqueous solutions of LiCl, $MgCl_2$, $Mg(NO_3)_2$, NaCl, KCl and KNO_3, which yielded RH of 11 %, 33 %, 54 %, 75 %, 85 % and 95 %, respectively, in sealed atmospheres at room temperature. These saturate salt solutions were placed in JKZ1 Radiosonde Ground Check to provide uniform and stable humidity environments. Capacitance of the MoS_2 and MoS_2@CuO were measured by the precision LCR Meter TH2817A with frequency of 100 Hz from China Tonghui. The variation of humidity environments will result in varying degrees of water molecules adsorption and thus generate different capacitances.

3. Result and discussion

Fig. 1a shows the XRD spectra of the pristine MoS_2 and MoS_2@CuO heterogenous structure. Black curve of MoS_2 can

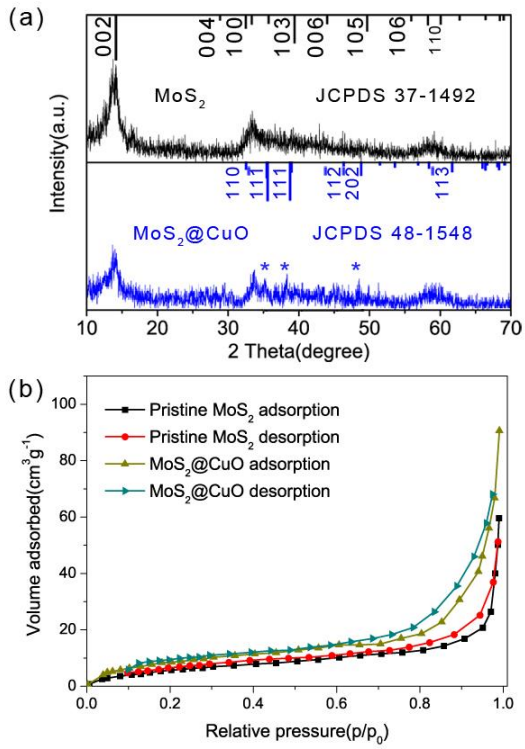

Fig. 1. (a) XRD patterns of the pristine MoS_2 and MoS_2@CuO heterogenous structure. (b) N_2 adsorption/desorption isotherms for the two samples.

be well indexed to the hexagonal phase of MoS_2 (JCPDS #37-1492) with lattice constants of a=b=3.16 Å, c=12.28 Å. The observed diffraction peaks around 14°, 33°, 40° and 59° can be well indexed to the (002), (100), (103) and (110) planes of hexagonal phase MoS_2, respectively. No other impurities peaks are found in the spectrum, indicating a high purity and crystalline of the pristine MoS_2 obtained. The MoS_2@CuO hetero-nanoflowers pattern is shown in blue curve, two different sets of lattice planes correspond to MoS_2 and CuO indicating that the composite structure is consisted by MoS_2 and CuO. However, it can be seen that the peaks around 35°, 38° and 48° attributed to CuO (JCPDS #48-1548) are relatively weak in comparison with MoS_2. This is because the highly crystallized MoS_2 structure may affect the peaks of CuO, which presents a small grain size and a low crystallinity. This phenomenon was also observed in the previous study of ZnO@CuO hybrid structure.[15] A further characterizations based on SEM, TEM, and XPS spectra will be conducted in the below sections to further characterize this heterogeneous structure in detail. In order to obtain the specific surface areas of the two structures, we draw two hysteresis loops under various relative pressures as shown in Fig. 1b. The Brunauer–Emmett–Teller (BET) surface area is 23.5 m^2g^{-1} for the MoS_2@CuO composite structure while 20.6 m^2g^{-1} for pristine MoS_2. This shows that the specific surface area of MoS_2@CuO composite structure is larger than that of pristine MoS_2.

Fig. 2 shows the morphology and microscopic structures of the pristine MoS_2 nanoflowers. The surface morphology of MoS_2 nanoflower can be clearly observed form SEM images at different magnifications of Fig. 2a and b. As exhibited in Fig.

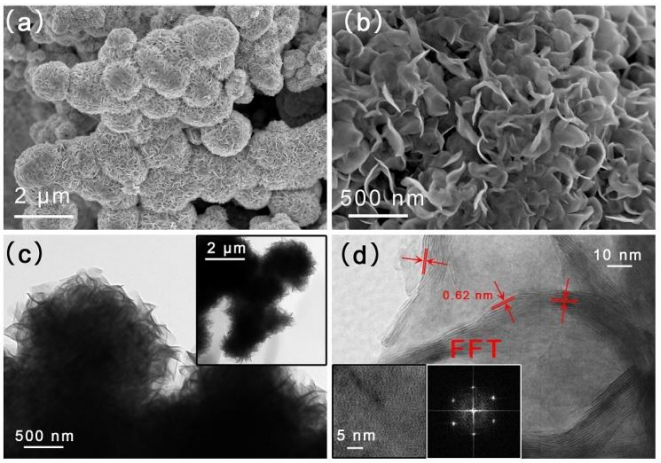

Fig. 2. (a) and (b) are low- and high-magnification SEM images of pristine MoS_2 nanoflowers, respectively. (c) TEM pattern of a MoS_2 nanoflower sphere. Insert shows low-magnification TEM image of the pristine MoS_2. (d) HRTEM image of a MoS_2 nanoflower petal. Insert shows FFT pattern of the corresponding HRTEM image.

2a, each MoS_2 nanoflower shows an average diameter of 1 to 2 μm. The surface of the MoS_2 nanoflower possesses a large amount of petals, which are freely and tightly aggregated together as displayed in Fig. 2b. The high-magnification of an individual MoS_2 spherical structure shows that the petals (2D nanosheet) disorderly intersected together and pointed toward a common inner center to form the spherical structure. It should be noted that each individual petal exhibits a curly and random growth method, this is obviously different from the following composite structure. In the Fig. 2c and d, TEM and HRTEM characterizations are conducted to further investigate the morphology and formation features of MoS_2 nanoflowers. Form the TEM image of Fig. 2c, it can be seen that the sphere is constructed by 2D MoS_2 thin layers. The low magnification of insert Fig. 2c shows MoS_2 spheres, it can be seen that the thickness of petals are about 100 nm, and these widely distributed petals can provide abundant active sites to take part in the corresponding chemical reactions. The high resolution TEM image of Fig. 2d shows that the fabricated petal structure is grown in high density way and has an interlayer separation of 0.62 nm. The lattice-resolved HRTEM image shown in insert Fig. 2d and the corresponding FFT pattern indicates the highly crystalline characteristic and undoubtedly attributes to MoS_2.

Fig. 3 shows the morphology and microscopic structures of the synthesized MoS_2@CuO hetero-structure nanoflowers characterized by SEM and TEM. Fig. 3a and b show the SEM images of the fabricated MoS_2@CuO hetero-nanoflowers composed by MoS_2 nanoflowers and CuO slices under different magnifications. Fig. 3a is the low-magnification SEM image, it can be seen that some light spots broadly distributed on the surfaces of MoS_2 spheres. Fig. 3b presents the high-magnification SEM image of the MoS_2@CuO hetero-structure, it is shown that the slice-like nanostructures of CuO are tightly inlayed into the different parts of MoS_2 petals and the thickness of CuO slices are about 60 nm. In contrast, the high-magnification SEM image of pristine MoS_2 petals displayed in Fig. 2b shows a freely and curving growth methods, which have

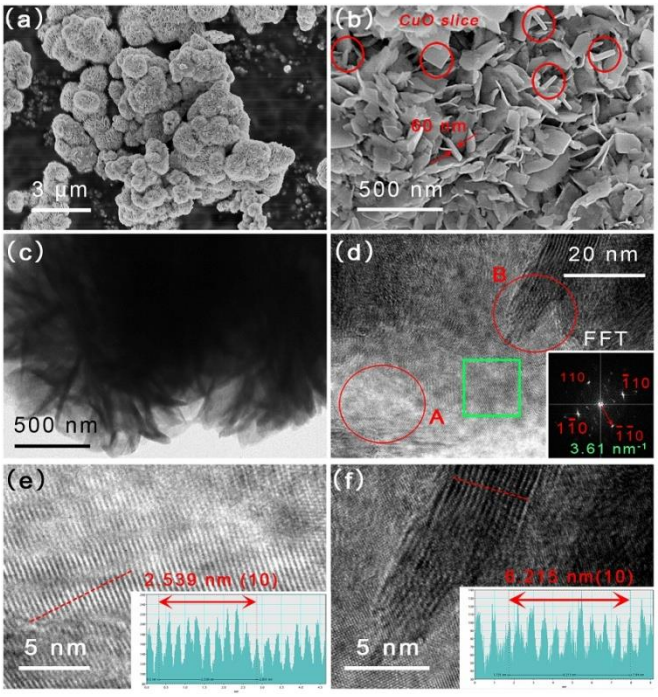

Fig. 3. (a) and (b) show low- and high-magnifications SEM images of the MoS_2@CuO hetero-nanoflowers, respectively. (c) TEM image of the composite structure. (d) High magnification TEM image of a MoS_2@CuO nanoflower petal, the two red circles A and B represent the HRTEM regions of (e) CuO slice and (f) MoS_2, respectively. Insert figure shows FFT pattern of the green square. Insert figures of (e) and (f) are intensity signals along the red dotted lines.

a clear distinction in comparison with the synthesized MoS_2@CuO hetero-structure.

As shown in the TEM image of MoS_2@CuO hetero-nanoflowers in Fig. 3c, the petals of the composite structure are also constructed by MoS_2 thin layers. Fig. 3d presents a HRTEM image for a combination region of MoS_2 and CuO, implying that MoS_2 petals and CuO nano-slices all have crystalline structures. Insert Fig. 3d shows FFT pattern of the green square. The bright spots with crystalline structure indexed unequivocally to CuO (JCPDS #48-1548). Fig. 3e and f show the lattice resolution images of regions A and B in Fig. 3d. In order to reduce biases, the atomic spacings of CuO and MoS_2 are obtained from the average values for 10 peaks. The inserted CuO slice exhibits lattice fringers of 0.2539 nm d-spacing which can be indexed to (002) plane, while the corresponding value for MoS_2 is 0.6215 nm attributed to (002) of MoS_2. In brief, MoS_2 nanoflowers and CuO heterogeneous structure can be clearly observed from Fig. 3a to d. It is apparently that for MoS_2@CuO hetero-nanoflowers, the MoS_2 petals are inserted by CuO slices and the corresponding hetero-nanoflowers formed. In conclusion, it is safe to assert that the formation of the 3D hierarchical MoS_2@CuO hetero-architecture through the corresponding analyses of SEM and TEM despite the XRD spectrum of the composite structure presents the relatively weak peaks of CuO.

According to Kraut's method,[16] the value of VBO can be calculated as:

$$\Delta E_v = (E^{MoS_2}_{Mo3d_{2/3}} - E^{MoS_2}_{VBM}) - [(E^{CuO}_{Cu2p_{1/2}} - E^{CuO}_{VBM}) - \Delta E_{CL}] \quad (1)$$

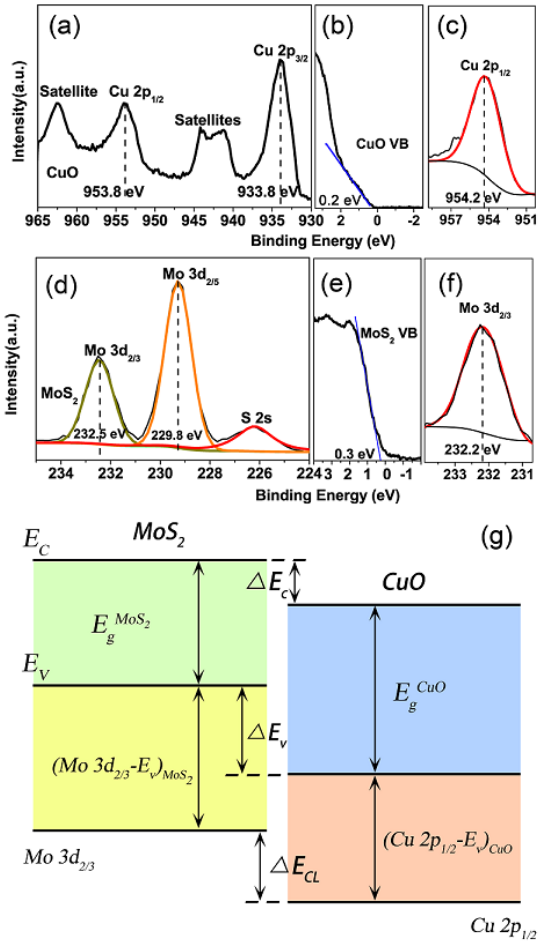

Fig. 4. (a), (b) and (c) are XPS spectra for Cu 2p, valence band (VB) spectrum of CuO and Cu 2p1/2 in MoS2@CuO heterostructure, respectively. (d), (e) and (f) are Mo 3d, VB spectrum of MoS_2 and Mo 3d2/3 of MoS_2@CuO heterostructure, respectively. Experimental data points are fitted by Voigt (mixed Lorentzian–Gaussian) line shapes after the application of a Shirley background. (g) Schematic diagram of band alignment of MoS_2@CuO heterojunction.

where $E^{MoS_2}_{Mo3d_{2/3}} - E^{MoS_2}_{VBM}$ and $E^{CuO}_{Cu2p_{1/2}} - E^{CuO}_{VBM}$ are the constants of pristine MoS_2 and CuO, VBM stands for valence band maximum. $\Delta E_{CL} = E^{MoS_2@CuO}_{Cu2p_{1/2}} - E^{MoS_2@CuO}_{Mo3d_{2/3}}$ is the band bending and should be measured in the heterojunction structures, representing the energy difference of core levels (CLs) between Cu $2p_{1/2}$ and Mo $3d_{2/3}$. The Cu $2p_{1/2}$ and Mo $3d_{2/3}$ XPS spectra of the different samples are plotted in Fig. 4a to f. For the Cu spectra of both the CuO and MoS_2@CuO samples, it show that the peaks corresponding to Cu 2p are identified, implying uniform bonding states established.[17] It is also observed the satellite peaks around 942 and 960 eV. The satellite effect is originated from multiple excitations that a valance electron is exited simultaneously when a core electron leaves the atom.[18] This effect is the characteristic of CuO corresponds to open d shell (d9) electron in the ground state.[19] For the spectra of both the MoS_2 and MoS_2@CuO, Mo $3d_{2/3}$ are also observed for the two structures. The VBM positions are obtained by linear extrapolation of the leading edges of XPS spectra to the base lines considering that the finite instrument precision.[20,21] The VBO value is calculated to be 0.6 eV by pluging those experiment values into Eq. (1). The CBO can be estimated by

the formula: $\Delta E_c = E_g^{MoS_2} - (E_g^{CuO} - \Delta E_{CL})$. Utilizing the reported band gap values ($E_g^{MoS_2}$ =1.3 eV, E_g^{CuO} =1.7 eV)[22, 23] , the ΔE_c is computed to be ~0.2 eV. According to the above calculated results, this undoubtedly implies the formation of staggered type-II band alignment for the MoS_2@CuO heterojunction.

Generally speaking, a staggered band alignment at the interface could bring about the electrons or/and holes trapped in the spike, which would incur the reduced surface photochemical activity. The accurate measurement of the band alignment by experiment of MoS_2@CuO indicates that the heterojunction structure shows staggered type-II band alignment and can provide an effective carrier separation in MoS_2 based photoelectric device. Compared with the other heterojunction photocatalysts, Yang et al.[24] investigated the VBOs of the Cu_2O-ZnO heterojunctions fabricated by magnetron sputtering through XPS analyses. The VBO/CBO of 2.91/1.71 eV and 2.52/1.32 eV were obtained for Cu_2O@ZnO and ZnO@Cu_2O heterojunctions, respectively. One thing to note is that Khanchandani et al.[25] designed ZnO@CdS as well as ZnO@Ag_2S core-shell nanostructures core-shell nanostructures with the same shell thickness. The results indicated that ZnO@Ag_2S core-shell nanostructures exhibited 40- and 2-fold MB degradation constant enhancement in comparison with the pure ZnO and ZnO@CdS core-shell nanostructures, respectively. A further study proved that the improved photocatalytic ability is ascribed to a smaller CBO between ZnO and Ag_2S, which could effectively promote the charge separation at the interface. In this work, the experimental values of VBO/CBO are relatively small, implying this MoS_2@CuO heterogeneous structure may also available for the photocatalysis usage.

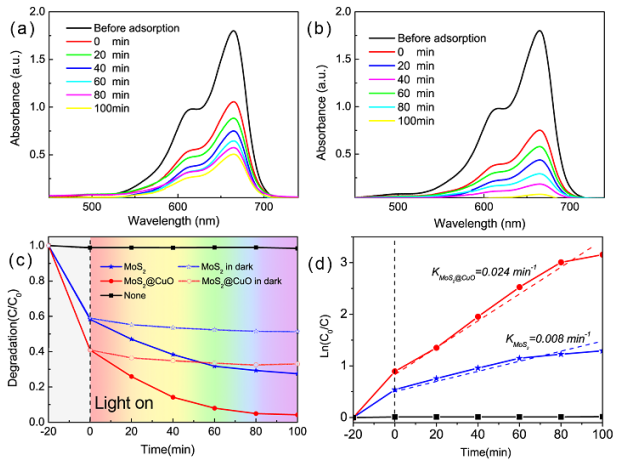

Fig. 5. (a) and (b) are UV-vis absorption spectra of MB solution after 100 min irradiation at room temperature in the presence of pristine MoS_2 and MoS_2@CuO hetero-nanostructure, respectively. (c) The normalized decrease concentration C/C_0 of the MB solution containing two catalysts with and without irradiation. (d) Logarithm (ln(C_0/C)) of the normalized concentrations vs. irradiation time.

Firstly, Fig. 5a shows the variation of absorption extracted form MB solution in the presence of the pristine MoS_2. The continually reduced absorption intensities at 664 nm signify the gradually decreased concentration of MB with increasing of the irradiation time. Fig. 5c presents the dependency of the degradation rate on irradiation time, in which C_0 and C are the initial and residual concentration of MB, respectively. A degradation of MB solution without photocatalyst is also conducted and almost no photocatalytic decolorization of MB solution after irradiating for 100 min as indicated in the black line of Fig. 5c. Also, no degradation of MB are observed when catalysts are added while no light is irradiated. These situations verify the stability of MB in the case of no light with catalyst or long time irradiation without catalyst. Accordingly, MoS_2 or MoS_2@CuO play a key role in the process of degradation under irradiation. One thing to note here is that before irradiation, the mixed solution of MoS_2 and MB are stirred for 20 min in dark to establish the adsorption/desorption equilibrium on the surfaces of MoS_2. The remaining MB concentration is about 60 % after equilibrium establishment, this may be ascribed to a large specific surface area can adsorb the dye molecules.[26] After irradiation for 100 min, C/C_0 significantly reduced to 27.5 %. The eminent photocatalytic performance of the pristine MoS_2 is attributed to the large specific surface area and the scraggly surface of the sample. It is widely believed that the larger specific surface area can enhance the adsorption of dye molecules and introduce more unsaturated coordination sites in the surface that exposed to MB molecules.

Daage[27] considered that the rim and edge sites of MoS_2 were the active sites based on the 'rim-edge' mode. Since every S or Mo atom coordinates two Mo atoms on the S-edge or four S atoms on the Mo-edge, respectively. S-edges have strong interaction with positively charged MB molecules for the unstable dangling bonds. Based on this consideration, the wrinkled surface with abundant defects or faults for MoS_2 nanoflowers can provide vast rims and edge active sites for the degradation of MB. Based on the above analyses, we infer that a certain amount of defects consist in the surface of the MoS_2 which can facilitate the formation of unsaturated S atoms and then the photodegradation of MB as shown in Fig. 6d.

For MoS_2@CuO hetero-nanoflowers, the corresponding absorption spectra are shown in Fig. 5b. As irradiation time increased, the MB solution containing MoS_2@CuO hetero-nanostructure presents a much faster peak-descending rate than that of pristine MoS_2 nanoflower. According to the above experiments, it is apparent that the photocatalytic ability of the MoS_2@CuO hetero-nanostructure is much better than that of the MoS_2 nanoflowers. After the dark adsorption/desorption equilibrium process, the remaining MB in solution is about 41 % for the MoS_2@CuO hetero-nanoflower, revealing MoS_2@CuO hetero-nanostructure possesses stronger specific surface area. After 100 min irradiation of the three samples under the same conditions, the degradation curves prove that MoS_2@CuO hetero-nanoflower possesses a better photocatalytic ability than that of the pristine MoS_2 nanoflowers, which originated from a different electronic transport mechanism. Besides, the curve of ln(C_0/C) versus time implies that MB photodegradation process followed pseudo-first order kinetics. On the basis of the Langmuir–Hinshelwood model,[28] the linear relationship of ln(C_0/C) versus

time can be described as: $\ln(C_0/C)=kt+A$, where k represents the photodegradation rate. For the different photocatalysts, the rate constant of pristine MoS_2 is 0.008 min^{-1}, while a higher rate constant of 0.024 min^{-1} is obtained for the MoS_2@CuO hetero-nanostructure.

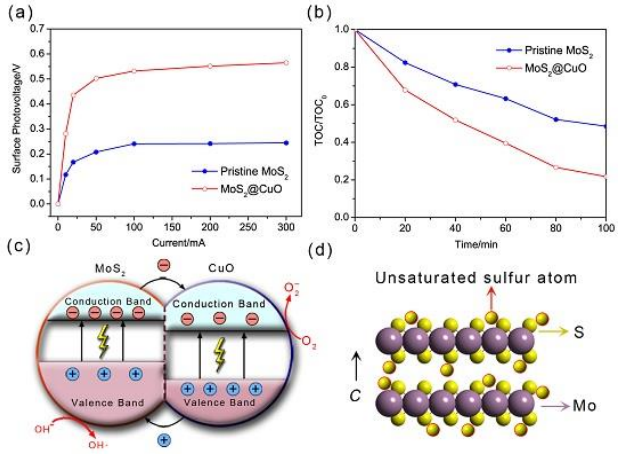

Fig. 6 (a) The average SPV values of pristine MoS_2 and MoS_2@CuO composite under various working currents. (b) Variation of TOC removal versus time for the MB dye solution. (c) Schematic diagram of the charge carriers (e-/h+) transfer mechanism in MoS_2@CuO. (d) Illustration of the unsaturated S atoms in MoS_2.

According to the above band offsets analyses and photodegradation experiments, the enhanced photocatalysis ability of MoS_2@CuO hetero-nanostructure can be ascribed to the specific charge-transfer kinetics. For the relatively narrow band gap of MoS_2, MB can be catalyzed by light illumination. Based on the formation of MoS_2@CuO hetero-nanostructure, the built-in electric field will facilitate separation of e^- and h^+. When the MoS_2@CuO hetero-nanostructure irradiated by UV-vis light, the photogenerated electrons and holes can separate efficiently at the interface and the photocatalytic ability get improvement for the reduced recombination rate.

In general, the photovoltage attributes to the separation of electron hole pairs under a built-in electric field and it can effectively reflect the photoinduced charge transfer and separation in the surface of the corresponding structure. According to Kronik et al. report,[29] a stronger SPV signal has positive correlation to a better charge separation efficiency and a higher photocatalytic activity. As shown in Fig. 6a, when the working current is higher than 50 mA, the average light-on SPV values of pristine MoS_2 exceeds 0.2 V, while higher values more than 0.5 V obtained for MoS_2@CuO composite. Therefore, it indicates that the formation of stagger type-II heterojunction exhibits a fast transfer of photogenerated electrons from MoS_2 to CuO slices and promotes the photogenerated electron–hole pairs separation and finally results in an improved photocatalytic performance.

In practical applications, some kinds of intermediate products in the relevant degradation processes are also toxic and thus the efficient mineralization of organic pollutants is crux for preventing secondary pollution.[30] Fig. 6b presents the changes of TOC during the photodegradation of MB after 100 min to study the mineralization abilities of the two catalysts. The TOC content decreased to ca. 21.7 % after 100 min of irradiation for composite which larger than that of the pristine MoS_2 of 48.6 %, implying most of the MB molecules can be mineralized through a photocatalytic process for MoS_2@CuO heterojunction.

After the separation of electrons and holes, the surface hydroxyl groups (or H_2O) capture the holes (h^+) of catalyst and generate $^{\bullet}OH$ radicals as shown in Fig. 6c. Besides, water molecules also can react with superoxide radical anions ($^{\bullet}O^{2-}$) that originated from the reaction between dissolved O_2 and electron to generate hydroperoxyl radicals ($HO_2^{\bullet}$). Finally, powerful oxidizing agents of oxydol (H_2O_2) and hydroxyl radicals ($OH^{\bullet}$) can effectively decompose the MB molecules. The related chemical reactions can be expressed as:

$$h^+ + H_2O \rightarrow H^+ + OH \quad (2)$$

$$e^- + O_2 \rightarrow {}^{\bullet}O^{2-} \quad (3)$$

$${}^{\bullet}O^{2-} + H_2O \rightarrow HO_2^{\bullet} + OH^- \quad (4)$$

$$HO_2^{\bullet} + H_2O \rightarrow H_2O_2 + OH^{\bullet} \quad (5)$$

$$H_2O_2 / OH^{\bullet} + organics \rightarrow \ldots \rightarrow CO_2 \uparrow + H_2O + \ldots \quad (6)$$

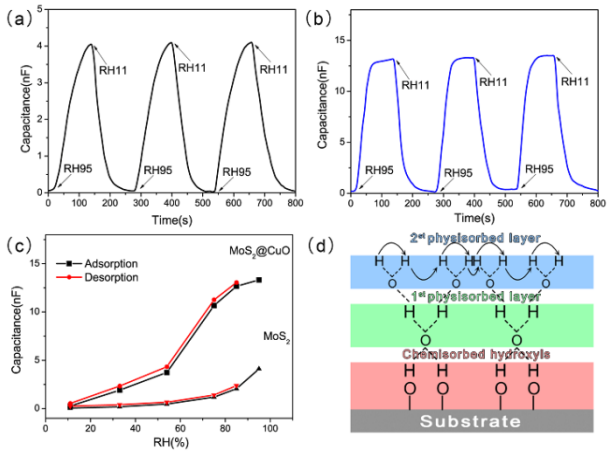

Fig. 7. Time-dependent capacitance of sensors based on (a) MoS_2 (black) and (b) MoS_2@CuO (blue) with RH switches from 11% to 95%. (c) Humidity hysteresis characteristics of MoS_2 and MoS_2@CuO humidity sensors measured at different RH. (d) Adsorption mechanism of water molecules.

The response/recovery times are the key characteristics to evaluate the humidity sensors' performance. Fig. 7a and b show the static response and recovery times for the adsorption and desorption curves of MoS_2 and MoS_2@CuO measured at room temperature. In this work, the time to achieve 95 % of the total capacitance change in adsorption or desorption process is defined as response or recovery time. The response time for MoS_2@CuO from 11 % to 95 % RH is 44 s, and the recovery time from 95 % to 11 % RH is 71 s, which are clearly better than that of MoS_2 (The response and recovery time of the MoS_2 structure are 102 and 83 s, respectively).

The relatively evident humidity hysteresis is also a key problem in the practical application of humidity sensors. The humidity hysteresis properties of the fabricated MoS_2 and MoS_2@CuO sensors are also measured in the range from 11 % to 95 % RH, and then in turn from 95 % to 11 % RH. As displayed in Fig. 7c, the hysteresis of MoS_2@CuO is slightly larger than that of MoS_2, this can be ascribed to a larger specific surface area of MoS_2@CuO in comparison with that of

MoS_2. A higher specific surface can render much more water molecules adsorbed on the surface of MoS_2@CuO nanostructure. Considering the mechanism of humidity sensing is based on adsorption, the reciprocities between water molecules and sensor can be summarized as two basic phenomenas: the formation of a chemically adsorbed layer of OH^- ions and protons at the surface of sensor, the subsequent formation of 1st physisorbed water molecules and the sequential condensation of free water at sensor' surface.[31] Based on this viewpoint, the hysteresis revealed a threshold process for the transition between two disparate sensing mechanism stages, which will be detailed discussed in below.

The humidity dependence of the capacitance for MoS_2 and MoS_2@CuO are described by the water separated layer adsorption mechanism, as shown in Fig. 7d. Generally, for the first layer of adsorption, the surface of fully dehydration MoS_2 nanostructure exists naked metal ion and negative sulfur ions. After the absorption of 1st water molecules, the H_2O ionized into OH^- and H^+ and the 1st chemisorbed layer is formed between OH^-/metal ion as well as H^+/ negative sulfur ions, making it possible for the other water molecule layer adsorbed through hydrogen bonding effect on OH^-. For the restriction of the two hydrogen bonding, it is incapable for the free movement of the 1st physisorbed absorbed water molecules. Therefore, the 1st physisorbed layer is immobile while no hydrogen bonds formed in this layer between the H_2O molecules. With the water molecules continue adsorbing on the surface of MoS_2 nanostructure, an additional H_2O molecule layer on top of the 1st physisorbed layer take shape. It should be noted that this adsorbed layer is less ordered than the 1st physically-adsorbed layer owing to the weaker bonding effect. It is noteworthy that as shown in Fig. 7c, the most significant change of the capacitance as the RH variation appears from 54 to 75 % RH for MoS_2@CuO hetero-nanostructure. According to this result, it is inferred that the 2nd or multi-physisorbed water molecules should be largely formed in this stage. Since the water molecules in the 2nd water layer and multilayer are orient freely and easy to be polarized with the external applied electric field. In consideration of the chemisorbed or 1st physisorbed water molecules provide only a limited contribution to the relative permittivity to increase the capacitance, the 2nd or/and multi-layers water finally lead to a significant increment of the corresponding relative permittivity and capacitance.[32] For the MoS_2@CuO composite structure, a higher specific surface can accelerate the first step of chemisorbed layer. Hence, the number of adsorption sites increased and it is benefit for the following adsorption of physisorbed H_2O molecules.

In conclusion, the improvement humidity sensitivity of MoS_2@CuO is preliminary attributed to a higher specific surface of MoS_2@CuO that results in an easier water adsorption. Nevertheless, it still cannot perfectly elucidate the increment of capacitance, since the adsorption ability of water molecules involving surfaces of MoS_2 and CuO is also an another crucial factor. As far as we know, there is still no report concerning H_2O adsorption on MoS_2 and CuO, so we conduct analyses based on the first-principles calculations in the following section.

4 Water molecule adsorption analysis

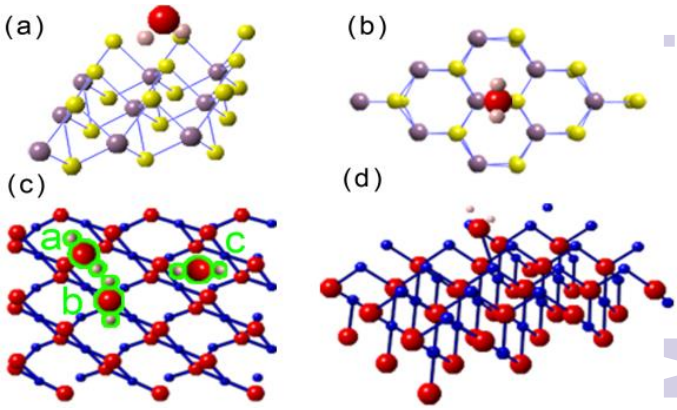

Fig. 8. (a) and (b) are the optimized geometry conformation of H_2O-MoS_2 from the top view and side views, respectively. (c) and (d) are primary geometry conformations of H_2O-CuO from the top and side views, respectively. A, B and C are the tentative adsorption sites.

In the following work, first-principles calculations are performed based on DFT with the projector-augmented wave (PAW) method implemented in the Vienna ab initio simulation package (VASP).[33, 34] The valence electrons considered are: Mo (p4s5d4), S (s2p4), O (s2p4), Cu (d10p1) and H (1s), respectively. The generalized gradient approximation (GGA) functional of Perdew, Burke and Ernzerhof (PBE) are employed to deal with the exchange and correlation potentials.[35] All calculations are performed with a $3\times3\times1$ supercell of H_2O adsorbed MoS_2/CuO systems. The spacing of 20 Å between two dimensional single layers of MoS_2/CuO was used to avoid interlayer interactions. A 6×6×1 Monkhorst–Pack k-point sampling for the Brillouin zone k-point mesh and a 500 eV cutoff energy are used for the calculations. The method of conjugate gradient energy minimization is used for geometry relaxation. The convergence criterion for energy between two consecutive steps is chosen to be 1E-4 eV, and for each atom upon ionic relaxation the maximum Hellmann–Feynman force is less than 0.02 eV/Å. The adsorption energy is defined as:[34] $E_{ads} = E_{Total} - E_{MoS_2/CuO} - E_{H_2O}$, in which E_{Total} is the energy of the surface with adsorbate optimized system, $E_{MoS_2/CuO}$ is the optimized energy and E_{H_2O} is the energy of a water molecule in free state.[36] According to this definition, a smaller E_{ads} value implies a more energetically favourable adsorption of water molecule on specific surface.

The energy of the above calculated structures are all calculated with the same unit cell size and $E_{cuttoff}$. The optimized geometry conformation of water molecule adsorbed on MoS_2 face determined by the above calculation is shown in Fig. 8a and b, in which the adsorbed nearest Mo or S atoms are indicated. With regard to the CuO adsorption model, we take three possible adsorption configurations into consideration: A, B and C. For the three configurations, we take C as the final choice for it has the lowest adsorption energy.

According to the above definition, the E_{ads} values of H_2O-MoS_2 is determined to be -0.086 eV, while E_{ads} values for H_2O-CuO is much more smaller than that of the former and determined to be -0.149. Generally, a lower adsorption energy

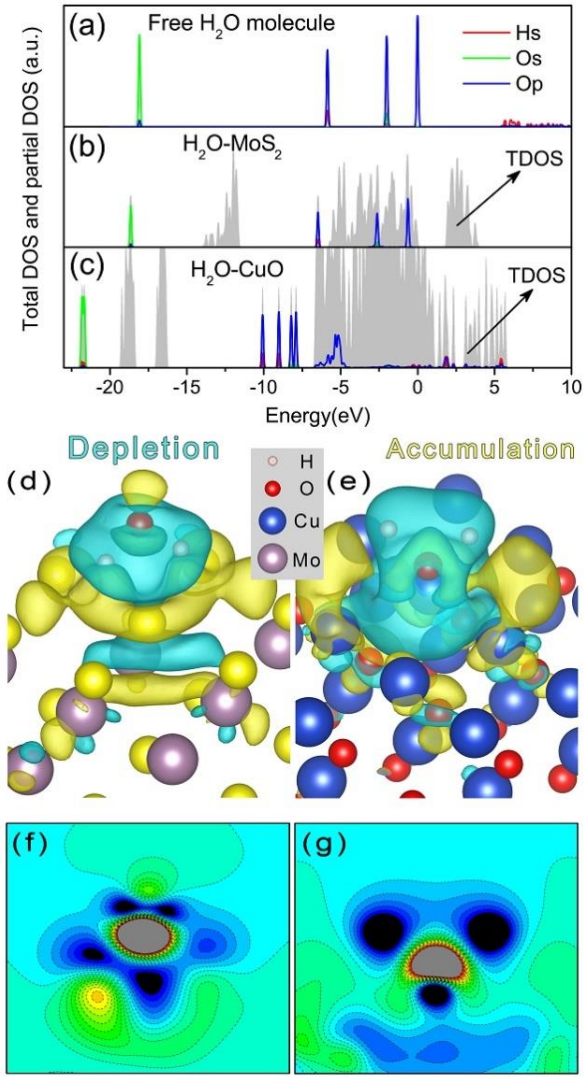

Fig. 9. (a), (b) and (c) are the total and partial DOS for H_2O, H_2O-MoS_2 and H_2O-CuO systems, respectively. (d) and (e) are the charge density difference maps for H_2O-MoS_2 and H_2O-CuO, respectively. Depletion and accumulation spaces are revealed in wathet blue and yellow, respectively. (f) and (g) are surface of the charge density difference contour for H_2O-MoS_2 and H_2O-CuO, respectively.

generally results in a strong binding between the adsorbate and host, forming a more stable composite configuration. It is indicated that there do have a stronger interaction between H_2O and CuO in comparison with H_2O and MoS_2. In consideration of this result, it looks that CuO should be more sensitive than MoS_2 when absorb water molecule. In order to further illustrate the adsorption effects of H_2O molecule on the electronic properties of MoS_2/ CuO, the total and partial DOS of MoS_2 and CuO are analyzed. The obtained results are presented in Fig. 9a to c. It can be seen that the DOS of free H_2O molecule is mainly comprised by two distinct regions: the deep region around -18 eV, which mainly originated from O 2s and a portion of 2p states; the shallower region of -7 to -0 eV mainly derived from O 2p states and the conduction bands dominated mainly by H s state. As for the H_2O-MoS_2 system, the PDOS for H_2O is slightly shift to lower energy direction, which is conform to the smaller adsorption energy that calculated above. However, the PDOS of H_2O adsorption on CuO results in a noticeable change. The integral DOS of H_2O obviously shifts to a lower energy direction.

This is attributed to the relatively larger adsorption energy and a stronger interaction between H_2O molecule and CuO substrate.[37]

To further qualitative analyze the charge transfer between adsorbed H_2O molecule and MoS_2/CuO systems, charge densities difference are shown in Fig. 9d and e. The charge density difference represents the charges re-distribution for the adsorbed system and the substrate along with the isolated adsorbate. As shown in the Fig. 9d, the yellow region represents charge accumulation while the blue represents charge depletion. From the charge density difference pattern of H_2O-MoS_2, it is exhibited that the major charge transfer happens between the two H atoms and its subjacent S atom. The yellow region between H and S atoms significantly larger than other parts, implying a certain amount of the charge transfer between these atoms. For H_2O-CuO system, there is an obvious change compared to H_2O-MoS_2, in which appears prominent depletion region. Fig. 9f and g show charge density difference contours of the two structures. According to contours, positive regions represent a gain of charge for the formation of the integral part and negative denote a loss of charge. It is evident that charge depletion/accumulation areas around H_2O molecule of H_2O-CuO system significant more than that of around H_2O-MoS_2. A preliminary deduction is that the charge transfer between H_2O-CuO may be more than that of H_2O-MoS_2, a further quantitative calculations based on Bader charge are conducted in the following.

Bader charge is usually applied to quantitatively calculate the electrons transferred between substrate and adsorbate for the adsorption system.[38] It is developed by Bader using the atoms-in-molecules approach.[39] For each atom *j*, a region of space Ω_j is distributed by trajectories of steepest density descent $(-\nabla n)$ and starting close to the nucleus. The Bader charge Q_j of atomic is expressed as $Q_j = Z_j - \int_{\Omega_j} n(\vec{r})d\vec{r}$, where Z_j is the nuclear charge of atom *j* (all electrons considered in the corresponding pseudopotential).[40] As calculated above that the significant differences of adsorption energies between H_2O-MoS_2 and H_2O-CuO, distinct differences are also reflected in the Bader charges. For H_2O-MoS_2 and H_2O-CuO two adsorption systems, the variation of Bader charges for the adsorbed H_2O molecule are 0.014 and 0.074 eV, respectively. Therefore, it shows different charge transfer degree when H_2O molecule adsorbed on MoS_2/CuO, which will result in different adsorption abilities as described above.

From the humidity sensitivity analyses of MoS_2 and MoS_2@CuO, the mechanisms of the composite structure exhibiting better humidity sensitive characteristics can be summarized from two aspects: The MoS_2@CuO structure show higher specific surface than that of pristine MoS_2, which can

bring more water adsorption sites and an increase of polarization/capacitance. Besides, stronger H_2O molecule adsorption characteristic is also an another key factor that influence the corresponding properties.

5 Conclusion

In conclusion, novel MoS_2@CuO hetero-nanoflowers were successfully synthesized by a two-step hydrothermal method. The VBO/CBO of MoS_2@CuO heterojunction were measured by XPS. It was found that the photocatalysts capacity of MoS_2@CuO heterogeneous structure was obviously more active than that of pristine MoS_2 nanoflowers through photocatalytic degradation of MB. The staggered type-II band alignment was believed to facilitate the design of MoS_2 and CuO based catalyst. The relatively small band offsets were significant for this heterojunction as neither photogenerated electrons nor holes were trapped, and both kinds of carriers could freely migrate to the surface and drive photocatalysis reaction. The humidity sensing properties improvement of MoS_2@CuO was attribute to a higher specific surface and a lower adsorption energy. First-principles calculations based on density functional theory (DFT) showed that the water molecule could adsorb on CuO in a more energetically favorable way in comparison with pristine MoS_2, leading to a better humidity sensing performance.

Acknowledgements

The authors acknowledge financial support from the NSF of China (Grant Nos. 61274014, 61474043, 61425004), Innovation Research Project of Shanghai Education Commission (Grant No. 13zz033) and Project of Key Laboratory of Polar Materials and Devices (Grant No. KFKT20140003).

1 R. Utpal and M. Sudip, *Chem. Commun*., 2012, **48**, 10862-10864.
2 J. Kang, J. B. Li, S. S. Li, J. B. Xia and L. W. Wang, *Nano Lett*., 2013, **13**, 5485–5490.
3 X. Y. Yu, S. P. Mathieu and S. M. Kevin, *Chem. Mater*., 2014, **26**, 5892–5899.
4 X. L. Fan, Y. Yang, P. Xiao and W. M. Lau, *J. Mater. Chem. A*, 2014, **2**, 20545-20551.
5 Y. F. Lim, C. S. Chua, C. J. Lee and D. Z. Chi, *Phys. Chem. Chem. Phys*., 2014, **16**, 25928-25934.
6 T. Chandan, S. Indranirekha, H. Moushumi and R. D. Manash, *RSC Adv*., 2014, **4**, 53229-53236.
7 G. P. Chen, D. M. Li, F. Li, Y. Z. Fan, H. F. Zhao, Y. H. Luo, R. C. Yu and Q. B Meng, *Applied Catalysis A: General*, 2012, **7**, 138-144.
8 M. D. Han, T. Sun, P. Y. Tan, X. F. Chen, O. K. Tan and M. S. Tse, *RSC Adv*., 2013, **3**, 24964-24970.
9 D. M. Geon, B. J. Ji, I. Lee and Y. D. Yin, *Nanoscale*, 2014, **6**, 12002-12008.
10 A. Zainelabdin, G. Amin, S. Zaman, O. Nur, J. Lu, L. Hultman and M. Willander, *J. Mater. Chem.*, 2012, **22**, 11583-11590.
11 Z. Y. Wang, Y. Xiao, X. B. Cui, P. F. Cheng, B. Wang, Y. Gao, X. W. Li, T. L. Yang, T. Zhang and G. Y. Lu, *ACS Appl. Mater. Interfaces*, 2014, **6**, 3888–3895.
12 H. Y. Guo, J. Chen, L. Tian, Q. Leng, Y. Xi and C. G. Hu, *ACS Appl. Mater. Interfaces*, 2014, **6**, 17184–17189.
13 N. P. Bhola and C. Dipankar, *Sensor. Actuat. B-Chem.*, 2006, **114**, 1043-1051.
14 J. S. Liu and L. J. Wang, *Sensor. Actuat. B-Chem*., 2014, **204**, 50-56.
15 J. Y. Kim, W. Kim and K. J. Yong, *J. Phys. Chem. C*, 2012, **116**, 15682 −15691
16 E. A. Kraut, R. W. Grant, J. R. Waldrop and S. P. Kowalczyk, *Phys. Rev. Lett*., 1980, **44**, 1620.
17 R. Widmer, F. J. Haug, P. Ruffieux, O. Gröning, M. Bielmann and P. Fasel. R. Gröning, *J. Am. Chem. Soc.*, 2006, **128**, 14103–14108.
18 T. Ghodselahi, M. A. Vesaghi, A. Shafiekhani, A. Baghizadeh and M. Lameii, *Appl. Surf. Sci*., 2008, **255**, 2730-2734.
19 S. J. Wang, J. W. Cai, J. S. Pan and A. C. H. Huan, *Appl. Phys. Lett*., 2006, **89**, 022105.
20 P. F. Zhang, X. L. Liu, R. Q. Zhang, H. B. Fan, H. P. Song, H. Y. Wei, C. M. Jiao, S. Y. Yang, Q. S. Zhu and Z. G. Wang, *Appl. Phys. Lett*., 2008, **92**, 042906.
21 T. D. Veal, P. D. C. King, S. A. Hatfield, L. R. Bailey, C. F. McConville, B. Martel, J. C. Moreno, E. Frayssinet, F. Semond and J. Z. Perez, *Appl. Phys. Lett*., 2008, **93**, 202108.
22 G. H. Li, N. M. Dimitrijevic, Le. Chen, T. J. Rajh and A. G. Kimberly, *J. Phys. Chem. C*, 2008, **112**, 19040–19044.
23 B. L. Li, L. X. Chen, H. L. Zou, J. L. Lei, Q. H. Luo and N. B. Li, *Nanoscale*, 2014, **6**, 9831-9838.
24 M. J. Yang, L. P. Zhu, Y. G. Li, L. Cao and Y. M. Guo, *J. Alloys Compd*., 2013, **578**, 143.
25 S. Khanchandani, P. K. Srivastava, S. Kumar, S. Ghosh and A. K. Ganguli, *Inorg. Chem*., 2014, **53**, 8902- 8912.
26 A. C. Power, A. J. Betts and J. F. Cassidy, *Analyst*. 2010, **135**, 1645-1652.
27 M. Daage and R. R. Chianelli, *J. Catal*. 1994, **149**, 414- 427.
28 S. X. Li, W. J. Liang, F. Y. Zheng, X. F. Lin and J. B. Cai, *Nanoscale*, 2014, **6**, 14254-14261.
29 L. Kronik and Y. Shapira, *Surf. Interface Anal*., 2001, **31**, 954-965.
30 Y. J. Chen, G. H. Tian, Y. H. Shi, Y. T. Xiao and H. G. Fu, *Applied Catalysis B: Environmental*, 2015, **164**, 40-47.
31 Y. H. Zhen, M. M. Wang, S. Wang and Q. Z. Xue, *Ceram. Int*., 2014, **40**, 10263-10267.
32 S. W. Chen, O. K. Khor, M. W. Liao and C. K. Chung, *Sensor. Actuat. B-Chem*., 2014, **199**, 384-388.
33 W. Huang, X. Luo, K. G. Chee, Y. Q. Su and G. Liang, *Phys. Chem. Chem. Phys*., 2014, **16**, 10866-10874.
34 T. Liang, S. W. Gregory, S. P. Scott, B. S. Susan and R. P. Simon, *J. Phys. Chem. C*, 2011, **115**, 10606–10616.
35 M. Kan, J. Y. Wang, X. W. Li, S. H. Zhagn, Y. W. Li, Y. Kawazoe, Q. Sun and P. Jena, *J. Phys. Chem. C*, 2014, **118**, 1515–1522.
36 S. J. Zhao, J. M. Xue and W. Kang, *Chem. Phys. Lett*., 2014, **595**, 35–42.
37 P. Cheng, S. L. Zhang, P. Wang, S. P. Huang and H. P. Tian, *Comput. Theor. Chem*., 2013, **1020**, 136-142.
38 J. Lee, Y. H. Kang, C. S. Hwang, S. W. Han, S. C. Lee and J. H. Choi, *J. Mater. Chem. C*, 2014, **2**, 8381-8387.
39 W. Tang, E. Sanville and G. Henkelman, *J. Phys.: Condens. Matter*, 2009, **21**, 084204.
40 G. Henkelman, A. Arnaldsson and H. Jónsson, *Comput. Mater. Sci*., 2006, **36**, 354-360.